UC Santa Cruz
UC Santa Cruz Previously Published Works

Title

High-Content Image-Based Screening and Deep Learning for the Detection of Anti-Inflammatory Drug Leads

Permalink

Journal

ISSN

Authors

Lau, Tannia A
Mair, Elmar
Rabbitts, Beverley M
et al.

Publication Date

DOI

High-content image-based screening and deep learning for the detection of anti-inflammatory drug leads

Tannia A. Lau[*,1], **Elmar Mair**[*,2], **Beverley M. Rabbitts**[*,1], **Akshar Lohith**[1], **R. Scott Lokey**[†,1]

[1]Department of Chemistry and Biochemistry, University of California Santa Cruz, Santa Cruz, CA 95064.

[2]No Affiliation, Santa Cruz, CA 95060

Abstract

We developed a high-content image-based screen that utilizes the pro-inflammatory stimulus lipopolysaccharide (LPS) and murine macrophages (RAW264.7) with the goals of identifying anti-inflammatory drug leads. We screened 2,259 bioactive compounds with annotated mechanisms of action (MOA) to identify compounds that block the LPS-induced phenotype in macrophages. We utilized a set of seven fluorescence microscopy probes to generate images that were used to train and optimize a deep neural network classifier to distinguish between unstimulated and LPS-stimulated macrophages. The top hits from the deep learning classifier were validated using a linear classifier trained on individual cells and subsequently investigated in a multiplexed cytokine secretion assay. All 12 hits significantly modulated the expression of at least one cytokine upon LPS stimulation. Seven of these were allosteric inhibitors of the mitogen-activated protein kinase kinase (MEK1/2) and showed distinct effects on cytokine expression, consistent with the complex pharmacology of MEK1/2 inhibition. This deep learning morphological assay identified compounds that modulate the innate immune response to LPS and may aid in identifying new anti-inflammatory drug leads.

Graphical Abstract

[†]Corresponding author.
[*]Authors contributed equally
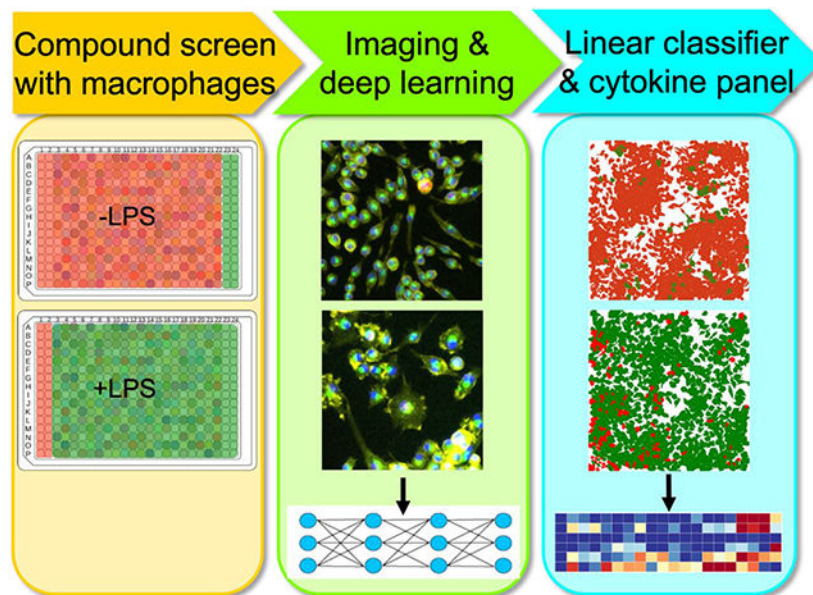
Introduction

Sepsis is a major health concern, causing profound morbidity and mortality worldwide. In the US alone, sepsis causes 270,000 deaths annually and is one of the leading causes of death in hospitals[1]. Sepsis is caused by the immune system's dysregulated response to infection, which can lead to an irreversible cascade culminating in shock and multiple organ failure. In the clinic, the management of sepsis has relied primarily on antibiotics and fluid administration[2], neither of which directly addresses the molecular events associated with immune hyperactivation. The high incidence and death rate associated with sepsis, and the lack of available treatment options, led the World Health Organization in 2017 to elevate sepsis to a global health priority.

During bacterial infection, lipopolysaccharide (LPS), a conserved lipoprotein from Gram negative bacteria, binds to the Toll-like receptor 4 (TLR4), which activates parallel intracellular inflammatory signaling pathways[3]. Hyperactivation of these pathways can cause an overwhelming release of cytokines such as iNOS, interleukins, and tumor necrosis factor alpha (TNF-a), leading to sepsis. The immortalized murine macrophage cell line RAW264.7 (RAW) can be stimulated by LPS to produce many of the morphological and molecular characteristics of the human innate immune response, thus providing a robust *in vitro* model system for investigating the innate immune response[4]. Upon LPS stimulation, RAW cells undergo significant physiological changes, including cytoskeletal changes, the production of nitric oxide (NO) and the release of pro-inflammatory cytokines.

Advances in automated microscopy and computer-aided image analysis have enabled high-content screening (HCS) approaches in which complex multiparametric phenotypic fingerprints are obtained from cells by quantifying images derived from a set of fluorescent probes. The distinct cytological effects of LPS stimulation on macrophages make HCS an attractive primary screening approach for identifying potential anti-inflammatory

compounds[5]. For example, a recent screen of a library of 2700 curated bioactives yielded modulators of the Stimulator of Interferon Genes (STING) pathway[6]. Machine learning approaches have also been applied to microscopy images to distinguish macrophage populations based on morphology[7, 8].

The most common methods for quantifying high-content screening data require the selection of features by the user based on computer-assisted segmentation of images into individual cells and/or cellular components. In contrast to these machine learning approaches, deep learning methods operate on raw images and do not require *a priori* analysis or segmentation. As computer processing and storage capabilities improve, deep learning approaches are being applied more commonly in the analysis of microscopy images[4, 9-18]. Deep learning approaches use machine-learning architectures with multiple layers that are trained to extract progressively higher-level features from raw images. The layers of filters are separated by nonlinear functions, and each layer combines the filter responses of its predecessor, resulting in progressively more complex features. While these types of neural network approaches have been used to evaluate immune cell phenotypes[19], thus far deep learning has not been applied toward the investigation of small molecule modulators of macrophage activation. Here, we develop a supervised deep convolutional neural network (CNN) classifier to identify compounds that inhibit induction of the LPS-stimulated phenotype in RAW cells (Fig. 1). The classifier was validated using standard cell-level segmentation-based methods, and the top hits were confirmed in a cytokine secretion assay. This approach provides a framework for identifying new potential anti-inflammatory leads, as well as compounds that can be used as chemical tools in the study of innate immunity.

Results

Primary high-content screen image collection

RAW macrophages were treated in 384-well format with a library of 2,259 bioactive compounds with annotated mechanisms of action (MOA) and stimulated with LPS. After 24 h of compound treatment, cells were fixed and stained using two sets of fluorescent probes: Stain Set 1 (ss1) consisted of probes for DNA, Golgi, actin, and mitosis, and Stain Set 2 (ss2) consisted of probes for DNA, tubulin, mitochondria, and DNA replication. As expected, the captured images revealed dramatic cellular feature changes in response to LPS stimulation: without stimulation, the cells appeared circular or elliptical, whereas LPS-stimulated cells appeared flattened and enlarged, with extensive filopodia protrusions (SI Fig. 1).

Optimizing input image format and CNN architecture

Deep learning models are computationally expensive and are often trained on relatively small images with side lengths of a few hundred pixels. In order to develop a CNN-based classifier that can automate detection of the LPS-induced phenotype, we set out to 1) find optimal image resolution and size parameters and 2) identify a CNN architecture that would enable classification with minimal computational resources. The initial images obtained from the automated microscope had side lengths of 1080 pixels. In order to build an

efficient CNN classifier that could be trained using our existing computational resources, the information content of each image had to be reduced significantly, either by cropping or reducing the image's resolution. In order to decide the best image reduction approach, i.e., the importance of detail (cropped, resolution retained) vs. context (not cropped, resolution reduced), we compared four different image modifications (Fig. 2A). To emphasize detail over context, we cropped the input image into sixteen 270 px (c270) or four 540 px (c540) images. To emphasize context over detail, we cropped the image into four 540 px and then resized those images to 270 px (cr540), or used the full-sized image of 1080 px, which was resized down to 270 px (r1080).

As CNN architectures increase in depth, memory consumption increases significantly, slowing down training and analysis. Therefore, shallow architectures are preferable, not only because they run faster and require less data for training, but also because they are less prone to overfitting, which can lower classification performance. Since the phenotypic expressions are at the cellular level, we hypothesized that it is not necessary for the CNN to capture details at various scales, which prompted us to develop a custom-built, shallow (3-layer) architecture. In one version of this architecture, each stain set was analyzed individually (Single Tower Model, STM) (Fig. 2B). In another version, a Siamese network was used to bring together both image stain sets (ss1+ss2) in a single head (Combined Tower Model, CTM) (Fig. 2C). We compared our custom-built shallow architectures (STM and CTM) to a baseline deep learning model called EfficientNet[20]. EfficientNet is a pre-trained model for image feature extraction, generated using a technique called "neural architecture search", which finds the optimal neural architecture for a specific task[21] (Fig. 2D). The classification performance of these CNN models will reveal the complexity of the CNN necessary for this task.

Training of deep neural network classifier

In order to identify the optimal combination of image reduction strategies and network architectures, we compared the accuracy of the 4 image resolution inputs using the STM (Fig. 2B) trained on individual stain sets (ss1 and ss2), the CTM trained on the combination of the stain sets (ss1+ss2) (Fig. 2C), and EfficientNet trained on the individual stain sets (Fig. 2D). The image reduction methods that emphasize context over detail, cr540 and r1080, showed the best performance for all of the network architectures, suggesting that images containing many, poorly resolved cells produce a better performing classifier than images with fewer, more highly resolved cells (Fig. 3A). The custom combined tower model (CTM) with both stain sets showed high accuracy among all of the input image resolutions (Fig. 3B), with a training set size of only 302 images being necessary to obtain an accuracy of 99% using the r1080 image reduction method. When trained on 700 or more images, high-performance models with ROC-AUC scores above 0.99 could be achieved using Stain Set #2 alone, indicating that the LPS-stimulated phenotype was captured effectively using generic cytological features that are not directly related to TLR4 signaling (Fig. 3C).

Dose response titration for hit validation.

To identify compounds that were able to block the LPS-induced phenotype, we ran the images from the 2,259 compound treatment wells in the presence of LPS through the

highest-performing CNN model as described above (CTM, r1080, 5632-image training set), with the goal of identifying wells that, upon LPS stimulation, are phenotypically similar to the unstimulated controls. The binary classification model assigns the unstimulated class a "deep learning" (DL) score of 0 and the LPS-stimulated class a score of 1; wells with DL scores between 0 and 0.01 were classified as hits. The CTM/r1080 model resulted in a total of 338 hits. We selected the top 19 hits from the deep learning classifier and investigated their effect on the LPS-stimulated phenotype in more detail. Since the primary CNN-based assay was designed to capture broad morphological changes upon LPS stimulation and did not include markers specific to the inflammatory signaling cascade, we introduced a probe for inducible nitric oxide synthase (iNOS), which is up-regulated upon LPS stimulation. The 19 top-scoring hits from the primary assay were tested in a secondary image-based microscopy assay at multiple doses ranging from 30 nM to 20 μM, using fluorescent stains for iNOS, DNA, and tubulin. While there was a clear difference in intensity in the iNOS stain between LPS-treated and untreated controls, surprisingly the compounds had little effect on iNOS levels in the LPS-stimulated wells (Fig. 4a).

As we had observed earlier in developing the deep learning model (Fig. 2), there were clear morphological differences in the DNA and tubulin channels between the LPS-treated and untreated conditions. Therefore, we trained a supervised linear classifier on the DNA and tubulin images from the LPS-stimulated vs. unstimulated controls, leaving the iNOS channel out of the analysis. This model captures the stimulated and unstimulated phenotypes at the cellular level, thus providing a measure of the fraction cells with the stimulated phenotype in each well. The LPS-treated controls showed ~80% of cells with the activated phenotype, whereas the non-LPS treated controls showed ~5% activated cells based on this model (these numbers were corroborated by visual inspection of the iNOS channel, which showed similar percentages of activated cells, i.e., cells with high iNOS expression, in the +LPS and –LPS controls, respectively). When this linear classifier was applied to the entire plate, 12 of the 19 compounds showed a significant decrease in the number of activated cells at any dose, while 8 compounds showed a significant decrease below 1 μM (Fig. 4b). The three most potent compounds, which showed a significant decrease in the number of activated cells as low as 30 nM, were lapatinib, TAK-733, and PD0325901. Lapatinib is a dual Erb2/EGFR tyrosine kinase inhibitor, while TAK-733 and PD0325901 are inhibitors of the mitogen activated kinases MAP2K1 and MAP2K2, also known as MEK1 and MEK2. Indeed, all 12 hits are annotated as kinase inhibitors, with 7 of the 12 hits being annotated as dual MEK1/2 inhibitors.

Effect of hits on LPS-induced cytokine expression.

In order to further evaluate their potential as anti-inflammatory agents, the 12 compounds that suppressed the LPS-stimulated phenotype based on the linear classifier described above were tested for their effect on a panel of 32 murine cytokines, chemokines and growth factors. RAW cells were treated with each of the 12 compounds for 4 h followed by treatment with LPS for 20 h, after which the supernatant was collected. Cells were treated with compound in triplicate at the following doses: 0.125, 0.375, 1.25, 3.75, and 10.125 uM. Controls included LPS + DMSO and DMSO alone. The 32 cytokines were measured simultaneously using the Luminex xMAP technology (Eve Technologies Corp., Calgary,

Alberta). Of the 32 cytokines in the panel, 15 showed a significant increase upon LPS stimulation. In addition to these, 4 cytokines whose levels were not affected by LPS alone were significantly modulated in the presence of at least one compound. All 12 compounds affected the expression of at least one cytokine in the presence of LPS manner, confirming the results of the deep learning model and secondary image-based linear classifier for identifying candidate anti-inflammatory modulators of the innate immune response (Fig. 5).

The MEK1/2 inhibitors all showed similar effects on cytokine secretion, decreasing levels of G-CSF, GM-CSF, IL1-alpha, IL1-beta, LIF, LIX, M-CSF, MIP-2, and TNF-alpha, and increasing secretion of IL-6, IL-10, KC, and RANTES. The cytokine profile of the MEK1/2 inhibitor U0126-EtOH was somewhat different from the other MEK1/2 inhibitors, for example, in its effect on RANTES and VEGF. This is perhaps not surprising given that U0126-EtOH is in a very different structural class, and is neither as potent nor as specific[22] as the other MEK1/2 inhibitors. We tested a subset of the MEK1/2 inhibitors for their effect on cytokine expression in the absence of LPS. For all three inhibitors (MEK162, U0126-EtOH, and PD0325901) none showed a significant effect on cytokine secretion in the absence of LPS (Supporting Information), thus demonstrating that the upregulation of IL-6, IL-10, KC, and RANTES upon treatment with these inhibitors was LPS-dependent. The two PI3K/MTOR inhibitors, GDC-0980 and PI-103, had similar effects on cytokine expression, while lapatinib, dasatinib, and TWS-119, which target EGFR, BCR-ABL, and glycogen synthase kinase-3β (GSK-33β), respectively, show distinct cytokine profiles, consistent with differences in their pharmacology.

Discussion

Here we describe the development of a deep-learning model that can distinguish between LPS-stimulated and unstimulated immune cells based on raw, high-content screening fluorescence microscopy images. The robustness of this model is not surprising given that stimulation with LPS induces a noticeable change in cell shape and nuclear morphology that was observed in nearly all the cytological probes used. Nonetheless, the highest-performing CNN model (CTM) is computationally expensive; alternative image analysis algorithms currently available, such as PhenoRipper[23] may be faster and advances in machine learning and artificial intelligence will undoubtedly increase the efficiency with which high content screening data can be analyzed.

Interestingly, while the iNOS channel gave distinct signals differentiating the LPS-stimulated vs. unstimulated controls, the effect of the compounds on iNOS levels was not consistent with their overall anti-inflammatory character based on their effect on cell morphology and, as confirmed later, their ability to modulate LPS-induced cytokine production. Since LPS has such an unambiguous and strong effect on cell morphology in these cells, we hypothesized that training a model on morphological features rather than a more targeted readout would cast a broad net and allow identification of compounds that impinge on any aspect of the cell's response to LPS. In retrospect, the weak effect on iNOS levels of many of the hits supports this original hypothesis.

Of the 19 top-scoring hits based on the deep learning classifier, 12 scored as anti-inflammatory in a conventional linear classifier follow-up assay. Since only these 12 were carried forward into the multiplexed cytokine expression assay, we do not know whether the remaining 7 were truly inactive or whether potential as anti-inflammatory agents were not captured by the follow-up assay. The differences between the deep learning assay and conventional linear classifier may indeed reveal compounds with different mechanisms of action and could both be useful as primary screens for anti-inflammatory agents.

All 12 of the hits that scored in the secondary assay are kinase inhibitors, and seven of those are selective for MEK1/2, central kinases in the signaling cascade that links TLR4 stimulation by LPS to the downstream upregulation of proinflammatory cytokines involved in innate immunity and sepsis. The RAS-RAF-MEK-ERK signaling axis drives cytokine production in macrophages upon LPS activation, and MEK1/2 inhibitors have been shown to block the release of cytokines and decrease mortality in mouse models of sepsis[24-27]. Studies have also demonstrated the effectiveness of MEK1/2 inhibitors in the treatment of autoimmune diseases such as collagen induced arthritis, rheumatoid arthritis, and lung diseases[25, 27-29].

In addition to the seven MEK1/2 inhibitors, five other kinase inhibitors also scored significantly in the secondary assay and modulated the expression of specific cytokines. These included the PI3K/MTOR inhibitors PI-103 and GDC-0980, the GSK3B inhibitor TWS-119, the EGFR inhibitor lapatinib, and the BCR-ABL/Src-family kinase inhibitor dasatinib. PI3K/MTOR dual inhibitors are known to modulate the release of the pro-inflammatory cytokines IL-1β, IL-6, IL-8, TNF-α, and G-CSF in macrophages upon LPS stimulation[30]. GSK3B is a central node in the signaling pathways linking TLR4 activation and cytokine expression, and TWS-119 has been shown to modulate production of pro-inflammatory cytokines in neurons in response to ischemic injury[31]. Likewise, dasatinib has been shown to decrease the expression of pro-inflammatory cytokines in neuronal cells challenged by LPS through the Akt/ERK signaling pathway[32], while EGFR inhibitors are also known to modulate LPS-dependent cytokine release in acute lung injury model in rats[33]. Thus, all 12 of the compounds that were selected based on their effect in the primary high-throughput assays showed a significant, dose-dependent effect on cytokine release in RAW cells, and their profiles of cytokine up- and down-regulation were similar for compounds in the same mechanistic class.

Conclusion

In this study, we demonstrate the feasibility of using raw images to train a convolutional deep learning neural network classifier to distinguish between LPS-stimulated vs. unstimulated macrophages. The algorithm was used to investigate the effect of a library of 2000 "known bioactives" (including tool compounds and clinically approved drugs) on the LPS-stimulated phenotype. Of the 19 compounds that scored the highest from the deep learning analysis, 12 inhibited the LPS-stimulated phenotype in a secondary screen using traditional segmentation analysis. All 12 compounds that scored in the secondary screen were kinase inhibitors, and of these, the majority were highly specific inhibitors of MEK1/2. MEK1/2 inhibitors are known to block signal transduction along the TLR4

pathway in stimulated macrophages, supporting the discriminatory ability of the original CNN model as well as confirming the results of the secondary assay. Therefore, it is possible to identify compounds that modulate the LPS response in macrophages based on cell morphology using deep learning screening approach, suggesting that such a model could be applied to the screening and analysis of a much larger library toward the discovery of novel anti-inflammatory agents.

Supplementary Material

Refer to Web version on PubMed Central for supplementary material.

Acknowledgements

Abbreviations

CCN	convolutional neural network
CTM	combined tower model
EdU	5-Ethynyl-2'-deoxyuridine
HCS	high-content screen
LPS	lipopolysaccharide
pHH3	histone H3 phospho-serine 10
RAW	RAW264.7 macrophage cell line
ss1	stain set 1 (probes for DNA, Golgi, actin, and mitosis)
ss2	stain set 2 (probes for DNA, tubulin, mitochondria, and DNA replication)

References

(1). Secreto C; Busca A; Lupia T; Corcione S; De Rosa FG The Management of Hematologic Patients with Bloodstream Infections Due to Multi-Drug Resistant Bacteria: Where Do We Stand? From Antibacterial Prophylaxis to the Treatment of Septic Shock. Hemato 2020, 1 (2), 60–76.

(2). Levy MM; Evans LE; Rhodes A The Surviving Sepsis Campaign Bundle: 2018 Update. Crit. Care Med 2018, 46 (6), 997–1000. DOI: 10.1097/CCM.0000000000003119. [PubMed: 29767636]

(3). Lu YC; Yeh WC; Ohashi PS LPS/TLR4 signal transduction pathway. Cytokine 2008, 42 (2), 145–151. DOI: 10.1016/j.cyto.2008.01.006. [PubMed: 18304834]

(4). Adams CL; Kutsyy V; Coleman DA; Cong G; Crompton AM; Elias KA; Oestreicher DR; Trautman JK; Vaisberg E Compound Classification Using Image-Based Cellular Phenotypes. In Measuring Biological Responses with Automated Microscopy, Methods in Enzymology, 2006; pp 440–468.

(5). Rodell CB; Koch PD; Weissleder R Screening for new macrophage therapeutics. Theranostics 2019, 9 (25), 7714–7729. DOI: 10.7150/thno.34421. [PubMed: 31695796]

(6). Koch PD; Miller HR; Yu G; Tallarico JA; Sorger PK; Wang Y; Feng Y; Thomas JR; Ross NT; Mitchison T A High Content Screen in Macrophages Identifies Small Molecule Modulators of STING-IRF3 and NFkB Signaling. ACS Chem. Biol 2018, 13 (4), 1066–1081. DOI: 10.1021/acschembio.7b01060. [PubMed: 29553248]

(7). Geng Y; Hardie J; Landis RF; Mas-Rosario JA; Chattopadhyay AN; Keshri P; Sun J; Rizzo EM; Gopalakrishnan S; Farkas ME; et al. High-content and high-throughput identification of macrophage polarization phenotypes. Chemical Science 2020, 11 (31), 8231–8239. DOI: 10.1039/d0sc02792h (acccessed 2021-02-24T18:37:15). [PubMed: 34123093]

(8). Rostam HM; Reynolds PM; Alexander MR; Gadegaard N; Ghaemmaghami AM Image based Machine Learning for identification of macrophage subsets. Sci. Rep 2017, 7 (1), 3521. DOI: 10.1038/s41598-017-03780-z. [PubMed: 28615717]

(9). Kraus OZ; Grys BT; Ba J; Chong Y; Frey BJ; Boone C; Andrews BJ Automated analysis of high-content microscopy data with deep learning. Mol. Syst. Biol 2017, 13 (4), 924. DOI: 10.15252/msb.20177551. [PubMed: 28420678]

(10). Parnamaa T; Parts L Accurate Classification of Protein Subcellular Localization from High-Throughput Microscopy Images Using Deep Learning. G3 (Bethesda) 2017, 7 (5), 1385–1392. DOI: 10.1534/g3.116.033654. [PubMed: 28391243]

(11). Durr O; Sick B Single-Cell Phenotype Classification Using Deep Convolutional Neural Networks. J Biomol Screen 2016, 21 (9), 998–1003. DOI: 10.1177/1087057116631284. [PubMed: 26950929]

(12). Sommer C; Hoefler R; Samwer M; Gerlich DW A deep learning and novelty detection framework for rapid phenotyping in high-content screening. Mol. Biol. Cell 2017, 28 (23), 3428–3436. DOI: 10.1091/mbc.E17-05-0333. [PubMed: 28954863]

(13). Godinez WJ; Hossain I; Lazic SE; Davies JW; Zhang X A multi-scale convolutional neural network for phenotyping high-content cellular images. Bioinformatics 2017, 33 (13), 2010–2019. DOI: 10.1093/bioinformatics/btx069. [PubMed: 28203779]

(14). Chandrasekaran SN; Ceulemans H; Boyd JD; Carpenter AE Image-based profiling for drug discovery: due for a machine-learning upgrade? Nat Rev Drug Discov 2021, 20 (2), 145–159. DOI: 10.1038/s41573-020-00117-w. [PubMed: 33353986]

(15). Hofmarcher M; Rumetshofer E; Clevert DA; Hochreiter S; Klambauer G Accurate Prediction of Biological Assays with High-Throughput Microscopy Images and Convolutional Networks. J. Chem. Inf. Model 2019, 59 (3), 1163–1171. DOI: 10.1021/acs.jcim.8b00670. [PubMed: 30840449]

(16). Scheeder C; Heigwer F; Boutros M Machine learning and image-based profiling in drug discovery. Curr Opin Syst Biol 2018, 10, 43–52. DOI: 10.1016/j.coisb.2018.05.004. [PubMed: 30159406]

(17). Simm J; Klambauer G; Arany A; Steijaert M; Wegner JK; Gustin E; Chupakhin V; Chong YT; Vialard J; Buijnsters P; et al. Repurposing High-Throughput Image Assays Enables Biological Activity Prediction for Drug Discovery. Cell Chem Biol 2018, 25 (5), 611–618 e613. DOI: 10.1016/j.chembiol.2018.01.015. [PubMed: 29503208]

(18). Kraus OZ; Ba JL; Frey BJ Classifying and segmenting microscopy images with deep multiple instance learning. Bioinformatics 2016, 32 (12), i52–i59. DOI: 10.1093/bioinformatics/btw252. [PubMed: 27307644]

(19). Severin Y; Hale BD; Mena J; Goslings D; Frey BM; Snijder B Multiplexed high-throughput immune cell imaging reveals molecular health-associated phenotypes. Sci Adv 2022, 8 (44), eabn5631. DOI: 10.1126/sciadv.abn5631. [PubMed: 36322666]

(20). Tan MX; Le QV EfficientNet: Rethinking Model Scaling for Convolutional Neural Networks. International Conference on Machine Learning, Vol 97 2019, 97.

(21). Elsken T; Metzen J; Hutter F Neural architecture search: A survey. arXiv 2018. arXiv preprint arXiv:1808.05377 2018.

(22). Duncia JV; Santella JB 3rd; Higley CA; Pitts WJ; Wityak J; Frietze WE; Rankin FW; Sun JH; Earl RA; Tabaka AC; et al. MEK inhibitors: the chemistry and biological activity of U0126,

its analogs, and cyclization products. Bioorg. Med. Chem. Lett 1998, 8 (20), 2839–2844. DOI: 10.1016/s0960-894x(98)00522-8. [PubMed: 9873633]

(23). Rajaram S; Pavie B; Wu LF; Altschuler SJ PhenoRipper: software for rapidly profiling microscopy images. Nat Methods 2012, 9 (7), 635–637. DOI: 10.1038/nmeth.2097. [PubMed: 22743764]

(24). Wang Y; Du P; Jiang D Rigosertib inhibits MEK1-ERK pathway and alleviates lipopolysaccharide-induced sepsis. Immun Inflamm Dis 2021, 9 (3), 991–999. DOI: 10.1002/iid3.458. [PubMed: 34061465]

(25). Shi-Lin D; Yuan X; Zhan S; Luo-Jia T; Chao-Yang T Trametinib, a novel MEK kinase inhibitor, suppresses lipopolysaccharide-induced tumor necrosis factor (TNF)-alpha production and endotoxin shock. Biochem. Biophys. Res. Commun 2015, 458 (3), 667–673. DOI: 10.1016/j.bbrc.2015.01.160. [PubMed: 25684183]

(26). Smith JA; Mayeux PR; Schnellmann RG Delayed Mitogen-Activated Protein Kinase/Extracellular Signal-Regulated Kinase Inhibition by Trametinib Attenuates Systemic Inflammatory Responses and Multiple Organ Injury in Murine Sepsis. Crit. Care Med 2016, 44 (8), e711–720. DOI: 10.1097/CCM.0000000000001672. [PubMed: 27031380]

(27). Jaffee BD; Manos EJ; Collins RJ; Czerniak PM; Favata MF; Magolda RL; Scherle PA; Trzaskos JM Inhibition of MAP kinase kinase (MEK) results in an anti-inflammatory response in vivo. Biochem. Biophys. Res. Commun 2000, 268 (2), 647–651. DOI: 10.1006/bbrc.2000.2184. [PubMed: 10679258]

(28). Long ME; Eddy WE; Gong KQ; Lovelace-Macon LL; McMahan RS; Charron J; Liles WC; Manicone AM MEK1/2 Inhibition Promotes Macrophage Reparative Properties. J. Immunol 2017, 198 (2), 862–872. DOI: 10.4049/jimmunol.1601059. [PubMed: 28003382]

(29). Bergqvist F; Sundstrom Y; Shang MM; Gunnarsson I; Lundberg IE; Sundstrom M; Jakobsson PJ; Berg L Anti-Inflammatory Properties of Chemical Probes in Human Whole Blood: Focus on Prostaglandin E2 Production. Front. Pharmacol 2020, 11, 613. DOI: 10.3389/fphar.2020.00613. [PubMed: 32435199]

(30). Xie S; Chen M; Yan B; He X; Chen X; Li D Identification of a role for the PI3K/AKT/mTOR signaling pathway in innate immune cells. PLoS One 2014, 9 (4), e94496. DOI: 10.1371/journal.pone.0094496. [PubMed: 24718556]

(31). Song D; Zhang X; Chen J; Liu X; Xue J; Zhang L; Lan X Wnt canonical pathway activator TWS119 drives microglial anti-inflammatory activation and facilitates neurological recovery following experimental stroke. J. Neuroinflammation 2019, 16 (1), 256. DOI: 10.1186/s12974-019-1660-8. [PubMed: 31810470]

(32). Ryu KY; Lee HJ; Woo H; Kang RJ; Han KM; Park H; Lee SM; Lee JY; Jeong YJ; Nam HW; et al. Dasatinib regulates LPS-induced microglial and astrocytic neuroinflammatory responses by inhibiting AKT/STAT3 signaling. J. Neuroinflammation 2019, 16 (1), 190. DOI: 10.1186/s12974-019-1561-x. [PubMed: 31655606]

(33). Shan X; Zhang Y; Chen H; Dong L; Wu B; Xu T; Hu J; Liu Z; Wang W; Wu L; et al. Inhibition of epidermal growth factor receptor attenuates LPS-induced inflammation and acute lung injury in rats. Oncotarget 2017, 8 (16), 26648–26661. DOI: 10.18632/oncotarget.15790. [PubMed: 28460454]
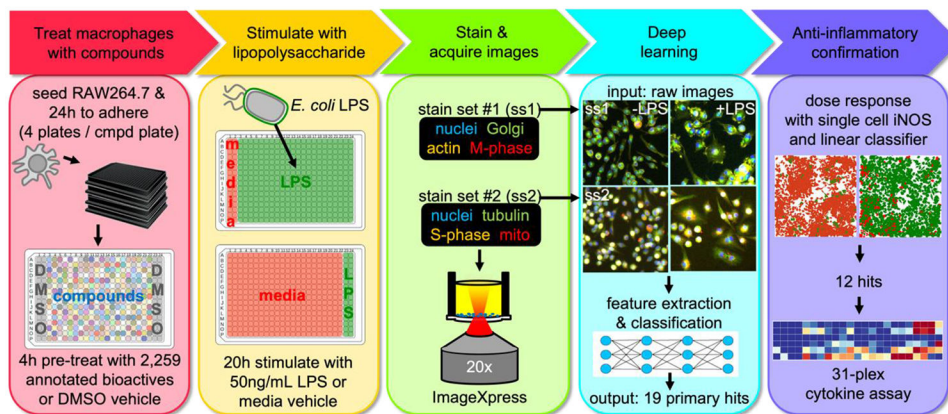
Figure 1. Workflow to identify anti-inflammatory hits using deep learning.
RAW264.7 cells adhered in 384-well plates were treated with chemical screening libraries or DMSO control for 4 h, then each plate either received media alone or media with 50ng/mL LPS for a further 20 h. Thus, each plate contains 64 non-drug-treated controls (32 unstimulated controls and 32 LPS-stimulated controls). The cells are fixed, processed, and stained with the established probes that target cell cycle, organelles, and cytoskeletal features. The images are used to train a deep neural network classifier on unstimulated and LPS-stimulated macrophages. Primary hit compounds that exhibit the unstimulated phenotype in the presence of LPS are selected for dose-response and cytokine assays.
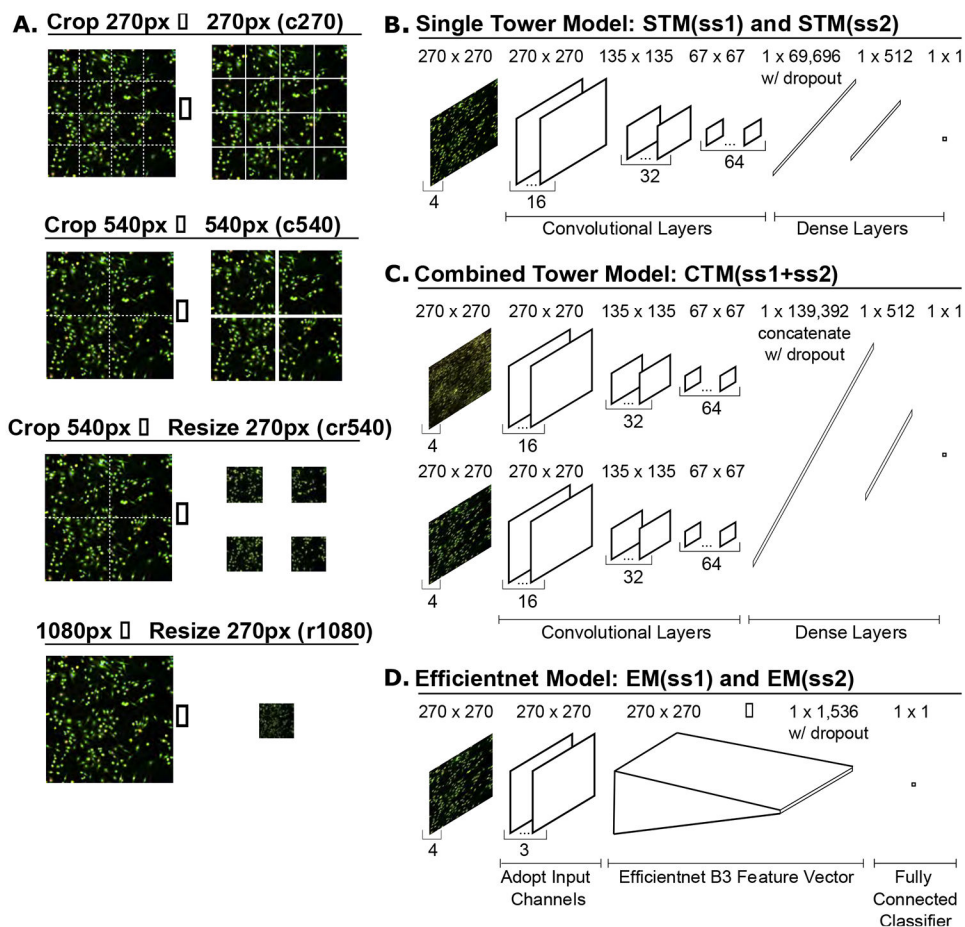
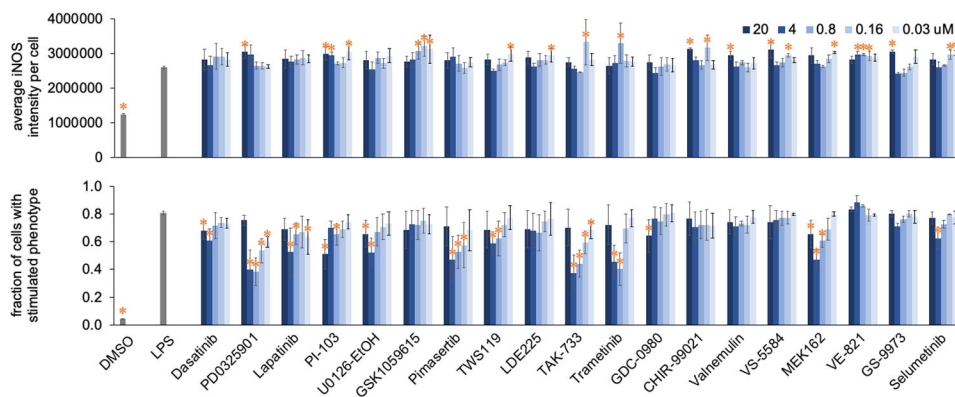**Figure 2. Deep learning parameters: image resolution and CNN models.**
A. Image resolution input format: starting with image size 1080 x 1080 pixels (px) that are cropped into sixteen: 270 x 270 px images (c270); cropped into four: 540x540px (c540); cropped into four: 540x540px and resized to 270x270px (cr270); and one: resized to 270x270px (r1080). **B.** Single Tower Model (STM) costume built simple 3-layer deep model that analyzes individual stain sets separately (ss1 and ss2) **C.** Combined Tower Model (CTM) a Siamese network which consists of a simple 3-layer tower and brings together both image stain sets (ss1+ss2) in a single head. **D.** EfficientNet Model (EM) is an image classification baseline model that analyzes individual stain sets separately (ss1 and ss2).
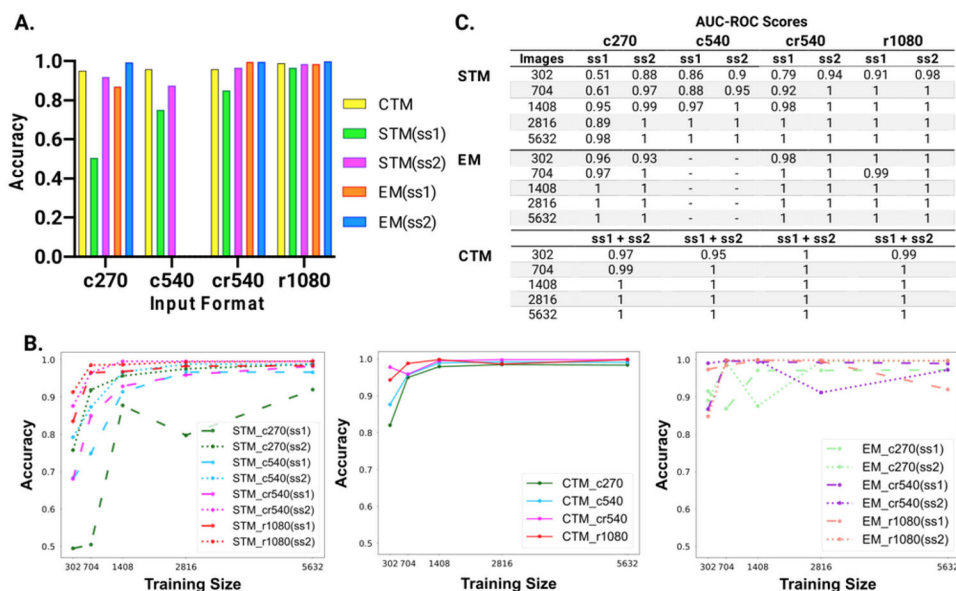
Figure 3. Best classification performance. Image resolution r1080 and cr540 and CNN architecture: CTM, EM(ss1), and EM(ss2).
**A.** Comparison of the classifier performance of varying image resolutions (c270, c540, cr540, r1080), models (STM, CTM, EM), and stain sets (ss1 and ss2). **B.** Comparison of the classifier performance on varying training dataset sizes. Training was performed on 302, 704, 2816, and 5632 images. **C.** Table summarizing the model classification confidence, measured by the Receiver Operating Characteristic (ROC curve) and Area Under the Curve (AUC) metrics. Data is split into 70:15:15. Each model is trained on 70% of the unstimulated and LPS-stimulated controls images, then 15% is for validation during training, and 15% is used for testing. Information for EfficientNet c540 (cropped 540 x 540px) is missing due to its high complexity and the lack of computational power. Training each model took from 1 to 3 hours depending on the architecture and the input format. We used two Nvidia GeForce GTX 1080Ti GPUs with two Intel Xenon E5-2640 (40 cores total).

AUC-ROC Scores

	Images	c270 ss1	c270 ss2	c540 ss1	c540 ss2	cr540 ss1	cr540 ss2	r1080 ss1	r1080 ss2
STM	302	0.51	0.88	0.86	0.9	0.79	0.94	0.91	0.98
	704	0.61	0.97	0.88	0.95	0.92	1	1	1
	1408	0.95	0.99	0.97	1	0.98	1	1	1
	2816	0.89	1	1	1	1	1	1	1
	5632	0.98	1	1	1	1	1	1	1
EM	302	0.96	0.93	-	-	0.98	1	1	1
	704	0.97	1	-	-	1	1	0.99	1
	1408	1	1	-	-	1	1	1	1
	2816	1	1	-	-	1	1	1	1
	5632	1	1	-	-	1	1	1	1
		ss1 + ss2		ss1 + ss2		ss1 + ss2		ss1 + ss2	
CTM	302	0.97		0.95		1		0.99	
	704	0.99		1		1		1	
	1408	1		1		1		1	
	2816	1		1		1		1	
	5632	1		1		1		1	

Figure 4. Dose-response of iNOS expression and linear classification of single cell phenotypes.
RAW264.7 macrophages were treated with compounds (or DMSO vehicle control) and LPS (or media vehicle control), fixed and stained for DNA, actin, and iNOS, imaged, segmented into nucleus and cytoplasm, and quantified at the single-cell level. Shown is the average and standard error of 3 biological replicate wells. Shown is the average and standard error of 3 biological replicate wells, with asterisk (*) showing those with t-test significance cutoff <0.01 as compared to LPS control. A. We quantified the sum of the intensity in the iNOS channel for all pixels within each cell, then averaged this across all cells in each well. B. We trained a linear classifier on iNOS-negative cells from unstimulated control wells and iNOS-positive cells from LPS as having the stimulated phenotype.
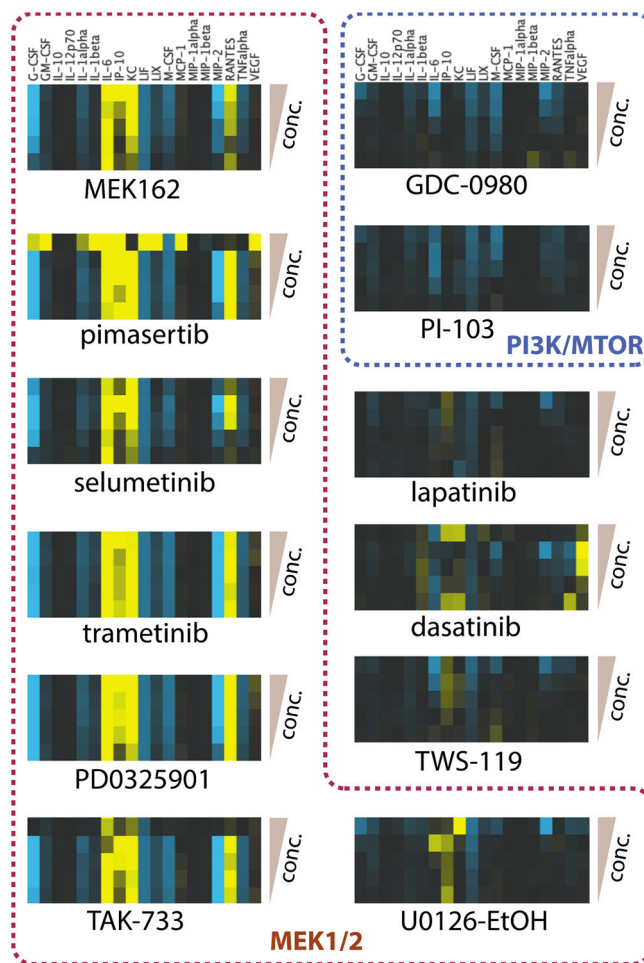
Figure 5.
Heat maps showing effect on cytokine secretion of the 12 hit compounds selected based on their effect in the linear classifier assay. Cells were treated with LPS plus compound under the conditions described above in the high-throughput assays, at 5 doses per compound: 0.125, 0.375, 1.25, 3.375, and 10.125 uM. Of the 32 cytokines measured, 19 showed a significant enhancement or depletion in the presence of drug. The cells in the heat maps represent the Z-scores, calculated as $(\mu_a - \mu_b)/\sigma_b$, where μ_a is the mean cytokine level in the presence of LPS plus drug, μ_b is the mean cytokine level in the presence of LPS plus DMSO, and σ_b is the standard deviation of the cytokine level in the presence of LPS plus DMSO. There were three biological replicates per treatment. The color range from blue to yellow represents a range of Z-scores from −5 to +5, respectively; thus, blue represents a decrease and yellow represents an increase in cytokine secretion in the presence of drug.